 CMES, vol.88, no.2, pp.107-138, 2012

The Design of Multi-Element Airfoils Through Multi-Objective Optimization Techniques

G. Trapani[1], **T. Kipouros**[1] **and A. M. Savill**[1]

Abstract: This paper presents the development and the application of a multi-objective optimization framework for the design of two-dimensional multi-element high-lift airfoils. An innovative and efficient optimization algorithm, namely Multi-Objective Tabu Search (MOTS), has been selected as core of the framework. The flow-field around the multi-element configuration is simulated using the commercial computational fluid dynamics (cfd) suite Ansys cfx. Elements shape and deployment settings have been considered as design variables in the optimization of the Garteur A310 airfoil, as presented here. A validation and verification process of the cfd simulation for the Garteur airfoil is performed using available wind tunnel data. Two design examples are presented in this study: a single-point optimization aiming at concurrently increasing the lift and drag performance of the test case at a fixed angle of attack and a multi-point optimization. The latter aims at introducing operational robustness and off-design performance into the design process. Finally, the performance of the MOTS algorithm is assessed by comparison with the leading NSGA-II (Non-dominated Sorting Genetic Algorithm) optimization strategy. An equivalent framework developed by the authors within the industrial sponsor environment is used for the comparison. To eliminate cfd solver dependencies three optimum solutions from the Pareto optimal set have been cross-validated. As a result of this study MOTS has been demonstrated to be an efficient and effective algorithm for aerodynamic optimizations.

Keywords: multi-objective optimization; tabu search; NSGA-II; high-lift airfoil design; robust optimization

[1] Department of Power and Propulsion - Cranfield University, Cranfield MK43 0AL, United Kingdom.

Nomenclature

δ_x	=	element deployment along the x-axis [m]
δ_y	=	element deployment along the y-axis [m]
θ	=	element deflection angle [°]
x, y	=	Cartesian coordinates
Re	=	Reynolds number
M_∞	=	freestream Mach number
cl	=	lift coefficient
cd	=	drag coefficient
cl_{max}	=	maximum lift coefficient
α	=	angle of attack [°]
α_{clmax}	=	stall angle of attack [°]
cp	=	pressure coefficient
c	=	stowed airfoil chord
L/D	=	lift to drag ratio
y^+	=	dimensionless wall distance
CoP	=	free form deformation control point

1 Introduction

The design of high-lift devices for civil aircraft has become increasingly important within the aerospace industry. Efficient high-lift configurations are, nowadays, fundamental to fulfill the increasing requirements in terms of aerodynamic efficiency and noise levels in near airport regions imposed by ICAO (Chapter 4 of Annex 16) [Greener by Design Science and Technology Sub-Group (2005)]. Although deployed only for short segments of an aircraft typical mission profile, relatively small changes in the aerodynamic performance of the high lift systems can produce large pay-off in airplane weight and performance [van Dam (2002)]. Moreover, these systems have a significant impact on the cost of a typical jet transport: they are time consuming and expensive to design and test; their flows, geometry, and actuation and support systems are complex; they are heavy and maintenance intensive [van Dam (2002)].

A broad range of different high-lift types has been developed over the years [Rudolph (1996)], although the most widely used in civil aircraft is the multi-element wing. This configuration is typically composed of a leading-edge device that increases the stall angle of attack, and a trailing-edge device that produces an upward shift in the lift curve. The positive effects of slotted flaps in increasing airfoil aerodynamic performance have been known for almost a century, but it was not until the 1970s that a theoretical basis for high-lift aerodynamics was made. This was a

result of the insight into the underlying physics of the highly complex flows involved provided by A.M.O. Smith [Smith (1975)]. The aerodynamic performance of multi-element wings is very sensitive to small variations in the gap size and the overlap between the various elements. Furthermore, the design of such system is made even more challenging by the requirement of retaining good performance level for a wide range of flap settings [van Dam (2002)].

The design of multi-element wings implies not only the design of the shape of leading and trailing edge devices but also the optimization of their relative positions. Wind tunnel tests are widely used during this phase to evaluate the aerodynamic performance of the configuration. However, the cost of such tests and the Reynolds number scaling problem (from wind tunnel to flight conditions) has lead to the development of alternative cfd tools to be integrated within the design process. In particular, RANS (Reynolds Averaged Navier-Stokes) tools, although still a subject of research, have been found to be reasonably reliable in predicting the aerodynamic performance of high-lift configurations. The use of RANS solvers in simulating the complex flow field around multi-element airfoils has been validated in the past [Lindblad and de Cock (1999); Rudnik, Eliasson, and Perraud (2005); Rumsey and Ying (2002); Fejtek (1997); Murayama and Yamamoto (2005)]. This validation process has enabled the application of numerical optimization methods to the design of high-lift configurations, making it an active area of research.

The European project EUROLIFT II [Amoignon, Quest, Moens, Quagliarella, Wild, and Brezillion (2007)] has promoted the assessment and comparison of several optimization strategies (gradient based, gradient-free and stochastic methods) combined with different RANS solvers. A common design problem was defined for a two-dimensional test case in landing configuration. All the involved partners approached the multi-objective problem using a single objective weighted function formulation. The only exception was CIRA, which used a multi-objective genetic algorithm (MOGA) combined with an Euler-boundary layer coupling code. Although widely used within the research community [Wild (1998); Wild (2008); Nemec, Zingg, and Pulliam (2004); Kim, Alonso, and Jameson (2002); Kroll, Gauger, Brezillon, Dwight, Fazzolari, Vollmer, Becker, Barnewitz, Schulz, and Hazra (2007); Besnard, Schmitz, Boscher, Garcia, and Cebeci (1998); Eyi, Lee, Rogers, and Kwak (1996)], the single objective weighted function formulation introduces designer biases into the optimization process: the value given to the weights of the different performance criteria considered. Besides, the use of true multi-objective algorithm has been limited to surrogate models based optimization. In particular, kriging models have been used in conjunction with a multi-objective preference based Particle Swarm algorithm by Carrese [Carrese, Winarto, Li, Sóbester, and Ebenezer (2012)] and in conjunction with MOGA by Kanazaki

[Kanazaki, Tanaka, Jeong, and Yamamoto (2007)].

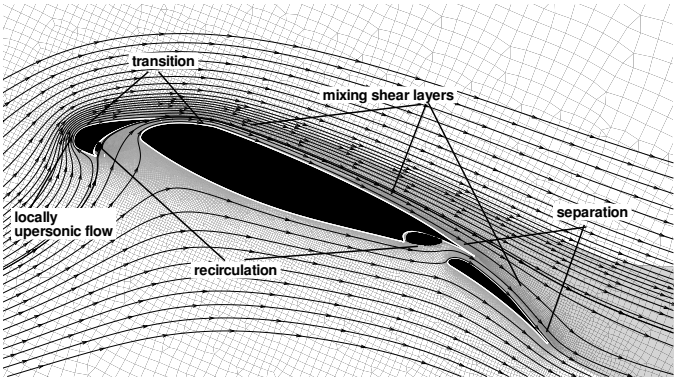

Figure 1: Visualization of flow-field around a multi-element wing [Wild (2008)]

The study presented in this paper combines the high fidelity resolution of the flow-field provided by RANS simulation with an innovative true multi-objective optimization algorithm MOTS. It is opinion of the authors that the characteristic blend between a local search and an heuristic approach of the MOTS algorithm provides an efficient strategy for the exhaustive exploration of the design space and the identification of the global optimum solutions.

The flow-field that develops around a typical multi-element configuration is shown in Fig. 1. It can be seen that additional complexity is present in the flow-field compared with a single element airfoil. In particular, recirculation areas develop in the cove regions of slat and main element, together with the mixing of the shear layers of the different elements. The complexity of the underlying aerodynamics and the sensitivity of the airfoil performance to the values of gap and overlap make the determination of the optimum positions of the elements a challenging task. That is why a framework has been developed for the automatic design optimization of 2D high-lift configuration deployment settings.

2 Description of the Optimization Framework

The optimization framework, illustrated in Fig. 2, comprises of both commercial and in-house developed software. The interfaces between the different modules have been implemented using c++ programming language and exploiting the journaling capabilities of the commercial software.

The stowed configuration (high lift devices retracted) represents the input geometry of the framework. A two-dimensional FFD (Free Form Deformation) technique

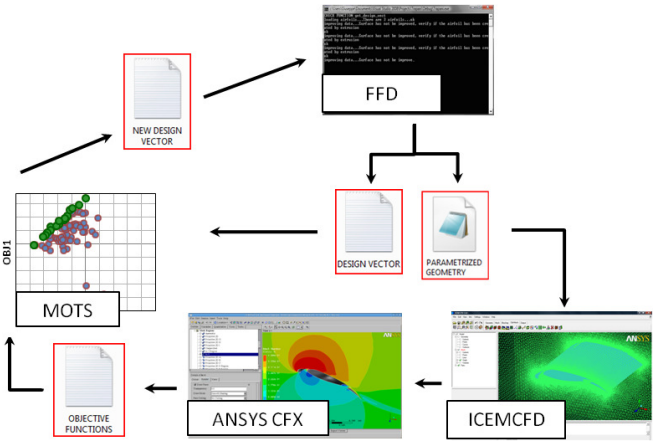

Figure 2: Optimization framework

based on the formulation of Sederberg and Parry [Sederberg and Parry (1986)] has been chosen to parameterize the elements of the high-lift airfoil. Following this technique a two-dimensional grid of control points is generated and super-imposed onto each element of the airfoil. The tensor product of trivariate Bernstein polynomial is then evaluated, relating each control point of the grid to the geometrical points of the airfoil. The modification of the position of any of the control point is, therefore, transferred to the geometry proportionally to the previously defined tensor. FFD has here been preferred to other parameterization strategies (e.g Non Uniform Rational B-Spline NURBS as used in [Diwakar, Srinath, and Mittal (2010)] or PARSEC as used in [Lian and Liou (2005)]), for its efficient manipulation of very complex geometries using only a limited number of control points.

The parameterized geometry is then loaded into the meshing tool Ansys Icemcfd, where the stowed configuration is deployed and the numerical mesh is generated. Checks are carried out on both the stowed and deployed configuration to avoid intersecting elements. The RANS flow simulation of the flow-field around the multi-element configuration is performed using the commercial suite Ansys cfx v5.0. The metrics of interest are extracted from the final cfd solution, combined to evaluate the objective functions and sent to the optimization algorithm together with the design variables values. Based on this evaluation the optimization tool-kit suggests a new configuration that is subsequently analyzed. The described loop continues until a stopping criterion is reached, e.g. evaluation time, number of iterations or residual increase in performance.

Table 1: Design variables range of variation.

Parameter	Description	Step	Range
Deployment Control			
Δx_S	Slat Translation along x, $\delta x/c$	0.02	$[-0.06; 0.14]$
Δy_S	Slat Translation along y, $\delta y/c$	0.01	$[-0.05; 0.09]$
Θ_S	Slat rotation, $\theta - \theta_0$	1°	$[-10.0^\circ; 10.0^\circ]$
Δx_F	Flap Translation along x, $\delta x/c$	0.02	$[-0.17; 0.09]$
Δy_F	Flap Translation along y, $\delta y/c$	0.01	$[-0.06; 0.00]$
Θ_F	Flap rotation, $\theta - \theta_0$	1°	$[-10.0^\circ; 10.0^\circ]$
Shape Control			
CoP	FFD selected control points, Δ/c	0.05	$[-0.2; 0.2]$

2.1 Design Variables

The deployment of multi-element wings is controlled by the so-called positioning parameters. Different coordinate systems can be used for the deflections of the devices, although the *Cartesian system* and the *gap-overlap definition* are the ones usually applied (see Fig. 3). Even though the latter notation is more related to the flow physics, the Cartesian system is more convenient for mathematical modeling and has been chosen in the presented study. Three variables are used to define the deployment settings of each element:

- δx: the distance along the x-axis between the trailing edge of an element and the leading edge of the following;
- δy: the distance along the y-axis between the trailing edge of an element and the leading edge of the following;
- θ: the angle within the chords of two consecutive elements.

In the practical parametrization process the first two parameters have been directly used as design variables. Instead, a new variable was used to express the deflection angle, defined as $\Theta = \theta - \theta_0$, where θ_0 is the deflection angle of the datum configuration. Hence, three design variables are needed to define the deployment of each element.

The free form deformation technique described in the previous chapter has been used to parameterize the shape of the flap element. Fig. 4(a) shows the generated control grid around the datum flap of the selected test case, while a deformation

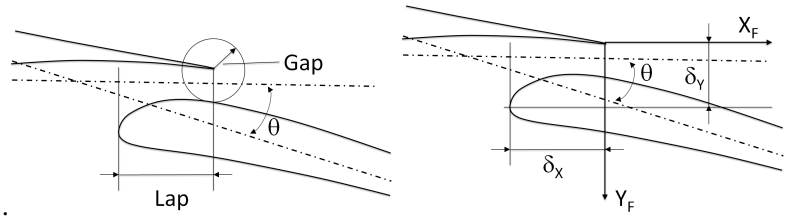

(a) Gap-lap definition (b) Cartesian system

Figure 3: Coordinate systems of high-lift device deployments [Wild (2008)].

example is presented in Fig. 4(b) . A total of 24 control points are used in order to be able to accurately define a local region where deformation occurs. In fact, it is an essential requirement in high lift design not to modify the shape of the stowed configuration in order to retain cruise performance. In the current study, flap shape changes have been confined to the area comprised between the flap leading edge and the suction side kink. Therefore, only the control points close to the specified region are allowed to move, as shown in Fig. 4(b), introducing six additional design variables:

- Δx only for the control points 1 and 2;
- Δx and Δy for the control point 3;
- Δy only for the control points 4 and 5.

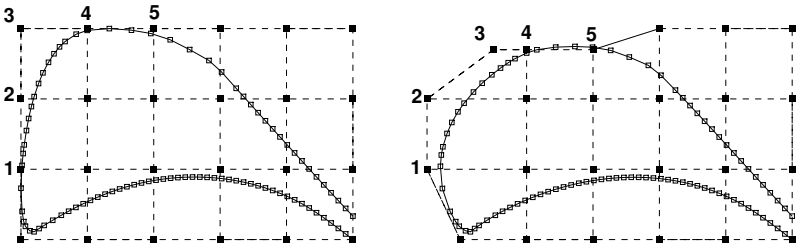

(a) Datum FFD Grid and Flap Geometry (b) Deformed FFD Grid and Flap Geometry

Figure 4: Example application of the Free Form Deformation algorithm.

In order to define the design space, i.e. the range of variability of the design variables, many different constraints should be considered. One of the most important

classes of constraints is represented by the kinematics used to deploy the high-lift devices. This aspect has an important influence on limiting the relative positions of slats and flaps in respect of the main element. Although, in the current study this class of constraints was not taken into account, the design space has been defined, for both slat and flap, keeping these limitations in mind. Tab. 1 presents the range of variations of the design variables, expressed in percentage of the chord. Finally, elements intersection checks are performed on the newly generated geometry to guarantee the feasibility of the design.

2.2 Grid Topology

A quad-dominant mesh has been used for the discretization of the flow-field around the multi-element configuration. Due to the complexity of the geometry an unstructured mesh approach has been preferred to a structure multi-block. The quad-dominant method presents various advantages compared with a pure unstructured triangular mesh. First of all, a reduction in mesh points can be obtained due to the geometrical definition (or shape) of the mesh elements, especially in the far-field region, where coarser mesh can be used. This approach introduces the opportunity of either reduce the simulation computational time (reduced mesh size) or increase the accuracy of the simulation introducing more mesh points in regions where the flow presents more complex phenomena. Furthermore, the obtained quad mesh presents a higher number of cells aligned with the main flow direction, reducing the numerical error of the solution.

Fig. 5 illustrates an example of the quad grid for a three-element airfoil. In order to better control the mesh points distribution the computational domain has been divided into three sub-regions: near-field, wake and far-field. In this way, a finer mesh can be used in the boundary layer and elements' wake regions to better resolve the underlying physics. The described approach generates a mesh with a total of approximately $260,000$ points with a First Cell Height (FCH) value of the order of $1e^{-6} \times c$ all around the airfoil boundaries. The low value of FCH is a requirement for the proper resolution of the boundary layer region and the correct application of the selected turbulence model of the cfd solver.

In this work the mesh generation approach has been preferred to the mesh deformation one, meaning that a new mesh is generated for each design evaluation. Therefore, the meshing process has to be automatically performed, requiring no input form the user. Moreover, it has to be robust since it has to be able to produce high quality mesh around a continuous changing geometry. The journaling capabilities of Icemcfd have been exploited to generate a script file containing the instructions that automatize the meshing process. To guarantee the accuracy of the simulation quality checks are automatically performed on the generated mesh before the flow-

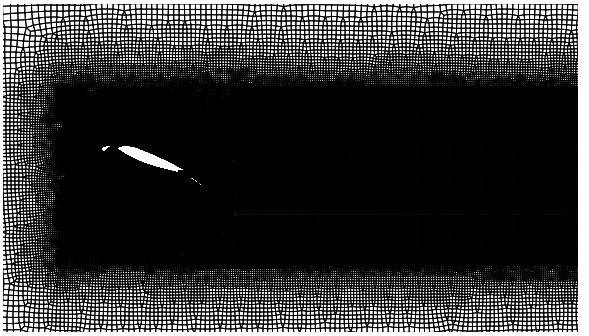

(a) Near-Field

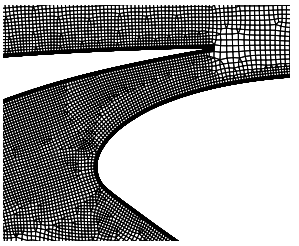

(b) Slat Slot Region

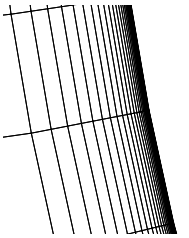

(c) Boundary Layer

Figure 5: Details of the quad-dominant mesh around a multi-element airfoil.

field evaluation. Meshes that present low-quality indicators are excluded from the evaluation and the correspondent design is marked as infeasible.

2.3 RANS Solver

The flow that develops around a multi-element airfoil represents a challenging numerical simulation, even when considering 2D configurations. The numerical solution must be able to capture accurately the mixing of boundary layers and wakes of preceding elements, the development of recirculation areas in the cutouts but also the occurrence of flow separation. This last requirement is fundamental if optimizations want to be performed for maximum lift conditions. Finally, although the free-stream Mach number M_∞ is relatively low, the flow can easily became transonic due to the high curvature imposed on the suction side by the slat element. Therefore, a compressible cfd solver is strongly recommended [Wild (2008)].

The commercial software selected in this work integrates the compressible unsteady RANS equations using a time-marching Second-Order Backward Euler scheme until a steady state solution is reached. The so called *High Resolution Scheme* is used for the discretization of the governing equations, resulting in both high accuracy and stability of the solution. The turbulence equations are, instead, solved using a first order method. The Mender Shear Stress Transport (SST) k-omega turbulence model has been chosen due to its superiority in capturing the occurrence of flow separation [Bardina, Huang, and Coakley (1997)]. To benefit from this model the boundary layer has to be well resolved, dictating the requirement for the dimensionless wall distance $y+$ value to be lower than unit on the airfoil's walls. Finally, the flow is considered to be fully turbulent on both lower and upper surfaces of the airfoil.

The final result of the simulation is achieved through the solution of the unsteady equations using a fictitious time-step. In order to avoid divergence behaviors and, hence, increase the robustness of the simulation, an increasing step function for the time-step has been used. Computational time has been reduced exploiting the built-in parallelization capability of Ansys cfx, executing each flow simulation on a four-processor node. Convergence checks are carried out at the end of each simulation in order to exclude any solution that presents oscillating or not converged behavior.

2.4 Optimization Algorithm

The selection of the optimization algorithm to implement within the framework has been driven by two main factors: the computational time of a flow evaluation and the nature of the design space. On the one hand, the first criteria implies that efficient algorithms that minimize the number of objective functions evaluations have to be used for time-consuming simulations. On the other, the presence of multiple local minima in a design space drives the need of an optimization algorithm that can widely search the design space and identify the so called *global optimum*. It is obvious the contrasting nature of such requirements.

Local search algorithms (e.g. gradient based) represent highly efficient optimization strategies but tend to be trapped in local minima. On the contrary, stochastic algorithms (e.g. Genetic Algorithm, Simulated Annealing, Tabu Search) are able to identify global optima but represent a heavier and less efficient optimization strategy. The Tabu Search algorithm has been chosen in this work due to its "intelligent" approach to the optimization process. The specific MOTS software has been developed by Jaeggi et al. [Jaeggi, Parks, Kipouros, and Clarkson (2008)] adapting the single-objective TS software implemented by Connor and Tilley [Connor and Tilley (1998)]. The TS algorithm can be seen as a further development and enhancement of a local search method. The Hooke and Jeeves local search algorithm is the core

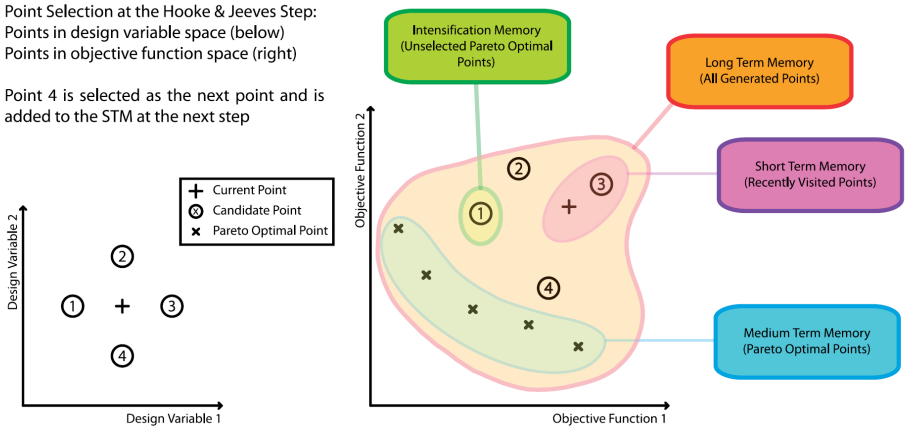

Figure 6: Point selection for the Hooke & Jeeves move and Tabu Search memories. Source: [Jaeggi, Parks, Kipouros, and Clarkson (2008)].

of the local search method used by TS. At each iteration $2n_{var}$ new points are created by the optimizer using a given step to increase $x_i + \delta_i$ and decrease $x_i - \delta_i$ the variable value. The objective functions are then evaluated for each new point and the best allowed (i.e. non-tabu and non-constraint violating) point is chosen as the next base point in the search.

Three main stages characterize the algorithm, each of which is associated with a particular memory allocation. Recently visited points are recorded in the *Short Term Memory* (STM), creating in such a way a Tabu list of points that will not be revisited. A *Medium Term Memory* (MTM) is used to store the optimal or near-optimal points which are used to perform the *Search Intensification* (SI) strategy. This consists in returning to a region that seems attractive and perform a more intense search but without revisiting the same solutions found. Search intensification occurs if there have been no successful moves for a defined number of local search iterations. While the SI intensifies the search of the optimum in one zone of the design space, the *Search Diversification* (SD) strategy moves the search to unvisited regions. A *Long Term Memory* (LTM) is used for this purpose, storing the areas which have been extensively searched by the optimizer. In order to perform such a move the design domain is divided in N sub-domain and the number of points visited in each sub-domain represent its visited index. When SD occurs the search is moved to a random sub-domain with a low visited index. Fig. 6 illustrates in a simple example the different memory categories of TS. The final stage of the algorithm is the *Step Size Reduction* (SSR) and occurs after a continued lack

of successful moves. This strategy is performed to ensure an intensive search in the neighborhood of the current optimal solutions. The step sizes of each design variable are reduced and the search returns to a randomly selected point from the MTM.

MOTS has been developed and proved to be particularly effective on aerodynamic problems [Harvey (2002)]. In [Connor and Tilley (1998)] the MOTS algorithm has been compared with a leading multi-objective genetic algorithm, NSGA-II [Deb, Pratap, Agarwal, and Meyarivan (2002)], showing that the two algorithms perform comparably. Moreover, the tool has successfully been used by Kipouros and Ghisu [Kipouros (2006); Jaeggi, Parks, Kipouros, and Clarkson (2008); Kipouros, Jaeggi, Dawes, Parks, Savill, and Clarkson (2008a); Kipouros, Jaeggi, Dawes, Parks, Savill, and Clarkson (2008b); Ghisu, Parks, Jarrett, and Clarkson (2011)] in the multi-objective optimization of axial compressors.

The algorithm has been coded using mpi (message passing interface) standards, so that the $2n_{var}$ generated designs can be evaluated in parallel. This feature, together with the parallel execution of the cfd analysis, allows a multi-level parallelization of the optimization process, resulting in a drastic reduction of the time to completion.

3 Validation and Verification of Cfd modeling

The high-lift configuration used throughout this work is the Garteur A310 airfoil [Flaig and Hilbig (1993)]. Reference wind tunnel tests carried out in the ONERA F1 wind tunnel are available [Manie, Piccini, and Ray (1989)] at a Reynolds number of $Re = 4.10^6$ and $M_\infty = 0.2$. The configuration comprises of a slat, a main airfoil, and a single-slotted flap as shown in Fig. 9. The moderate deployment settings are characteristic of a take-off configuration.

A validation and verification study of the cfd simulation has been performed comparing the available experimental data and the numerical solutions. Due to the confidentiality of the data the absolute values cannot be presented here. Three different meshes with increasing cell numbers have been generated and used to obtain the lift and drag coefficients at a fixed angle of attack. The obtained data has been compared with wind tunnel tests for the same flow settings. The results are shown in Fig. 7, where it can be seen that the numerical error reduces with increasing mesh size. Moreover, a comparison of numerical evaluated and experimental polars is shown in Fig. 8. The cfd simulation satisfactorily predicts the aerodynamic performance of the airfoil for the whole range of angle of attacks. In the near-stall region the numerical solution slightly under-predicts both the cl_{max} and the α_{clmax} values. A direct comparison of the drag coefficient cannot be made due to the inconsistency of the experimental data (pressure tabs measurement versus wake

survey). However, the numerical solution achieves values of c_d that fall between the two experimental curves.

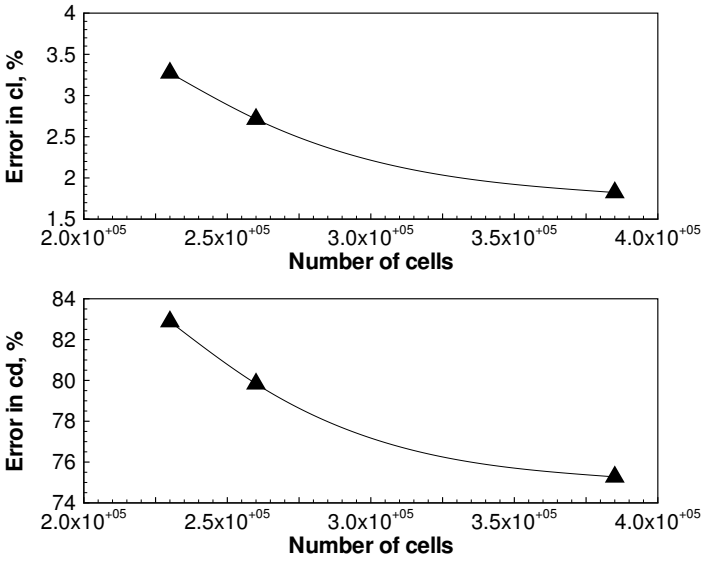

Figure 7: Mesh convergence study at moderate angle of attack.

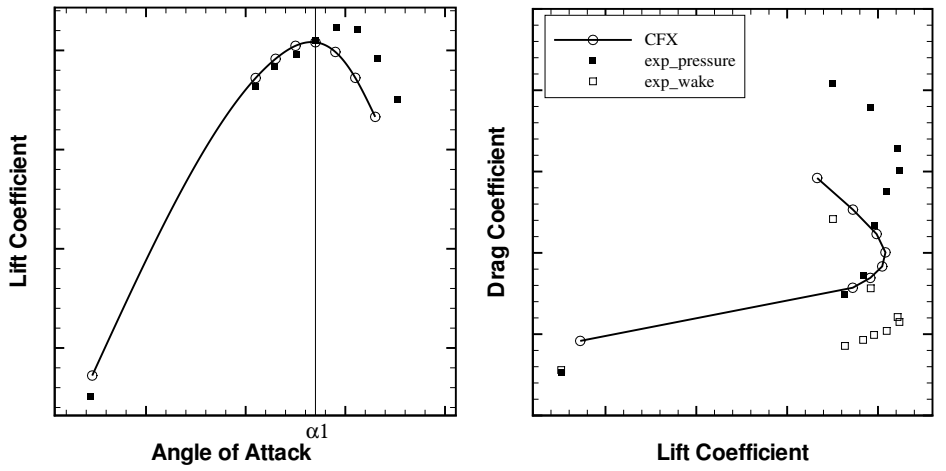

Figure 8: $cl - \alpha$ and $cd - cl$ polars comparison. Numerical results and wind tunnel data.

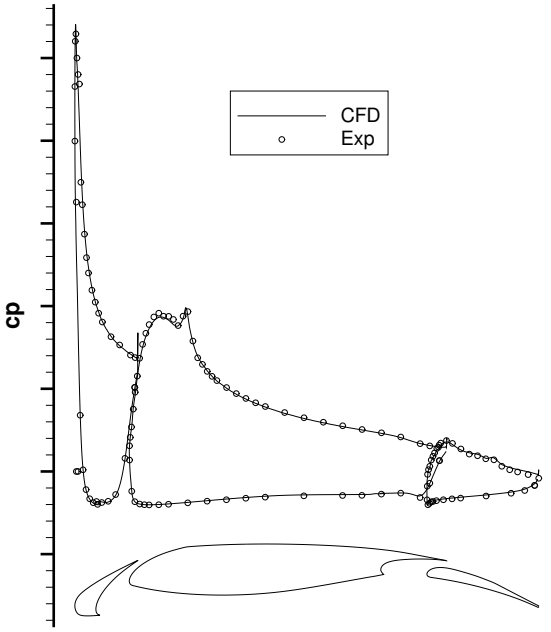

Figure 9: Wind tunnel and numerical pressure distributions.

Pressure distribution comparison over the airfoil is presented in Fig. 9. The numerical solution accurately matches the wind tunnel data, although a slight mismatch in the pressure coefficient is shown on the slat element. The wind tunnel data shows the presence of a transition bubble on the suction side of the slat element. The numerical simulation cannot capture such phenomena, since the flow is considered to be fully turbulent.

Prior to the set-up of the optimization process the convergence behavior of the numerical solution has been analyzed in order to identify the minimum number of iterations required to achieve a converged solution. Fig. 10 shows the evolution of the residuals and the aerodynamic coefficients during the simulation at the numerical maximum angle of attack condition α_1. After 160 iterations the residuals of the solution converged to a value of $1e^{-6}$ and both the aerodynamic coefficients present converged behavior. However, to allow the optimizer to explore configuration with harder convergence behavior the iteration threshold has been set to 250.

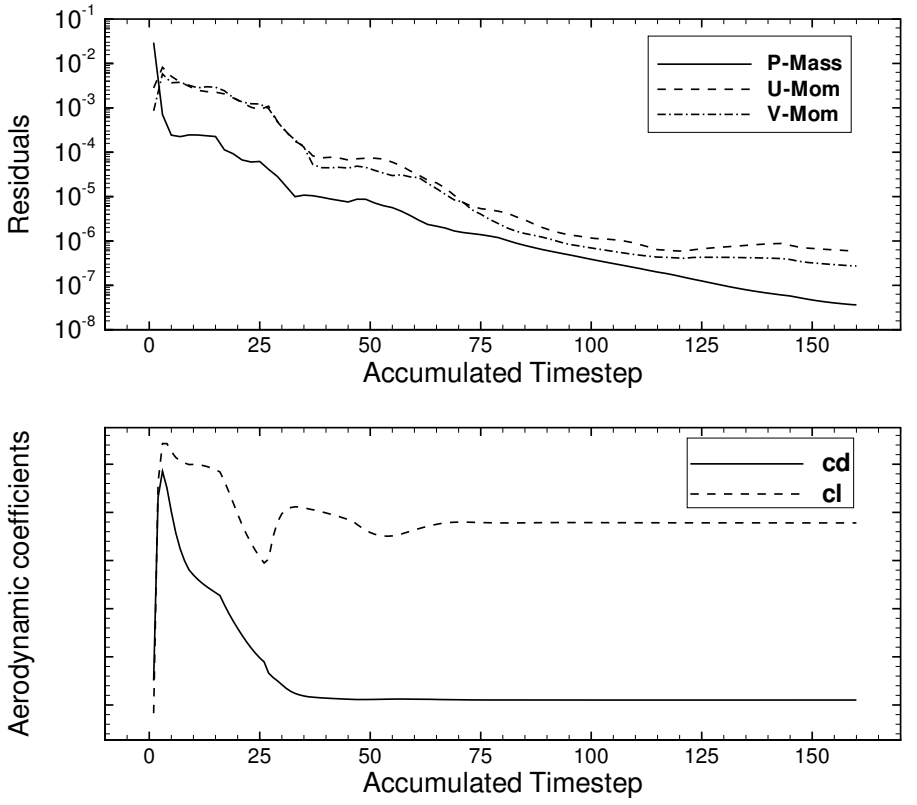

Figure 10: Datum design convergence monitor for the numerical solution at α_{clmax}

4 Problem formulation

The design of high-lift configuration is a complex and challenging task requiring the simultaneous satisfaction of several conflicting requirements. It is indeed a multi-objective problem. For this reasons any numerical optimization strategy that aims at supporting the design process needs to take this characteristic into account. In general mathematical terms a multi-objective optimization problem can be expressed as:

$$\begin{aligned} &\text{minimize} \quad f(x) = \{f_1(x), ..., f_n(x)\}, x \in R^n \\ &\text{subject to} \quad \begin{cases} c_i = 0, i = 1, 2, ..., m' \\ c_i \geq 0, i = m' + 1, ..., m \end{cases} \end{aligned} \tag{1}$$

where $f(x)$ are defined as the objective functions, x is the vector containing the *design variables* and c_i is the set of constraints to which $f(x)$ are subjected. Finding a solution to this problem means to determine a set of design variables that minimize the value of the objective functions satisfying, at the same time, the constraints. Unlike single optimization problems where a unique optimum solution is clearly defined, this problem is characterized by a family of alternative solutions and the concept of *Pareto-optimality* must be introduced. Originally postulated by Ysidro Edgeworth in 1881 [Edgeworth (1881)] and generalized afterwards by Vilfredo Pareto [Pareto (1896)] it states that a solution is *Pareto optimal* if no other feasible solution exists which would simultaneously improve all of the objective functions. The set of all the solutions that satisfy this requirement is defined as *Pareto optimal set* and consists of all the non-dominated solutions. The corresponding objective functions representation is instead defined *Pareto Front*. Those two concepts are fundamental when dealing with multi-objective optimization and will recur in this study when analyzing the numerical results obtained.

The formulation of the design optimizations performed by the authors in this study is here presented. The *single-point* design problem aims at concurrently minimize the two objective functions given by the following equations:

$$\text{obj1} = -\frac{cl}{cl_0} \quad ; \quad \text{obj2} = \frac{cd}{cd_0} \tag{2}$$

where the subscript 0 indicates datum design values. The value of the aerodynamic coefficients in Eq. 2 are evaluated at the angle of attack at which the datum configuration achieves its numerical maximum lift. The optimization is, therefore, performed at a fixed angle of attack, indicated as α_1 (see Fig. 8). The deployment settings of the slat and flap elements are considered as design variables, adding up to a total of six. Hard constraints have been applied on the design variables to exclude zero gap configurations from the optimization process.

The use of numerical optimization techniques in aerodynamic design can provide notable increase in performance for the specified design conditions. However, the identified optima are often very sensitive to small variations in manufacturing tolerances and/or operating conditions [Huyse, Padula, Lewis, and Wu (2002)]. As a result, the optimized design could present inferior performance under actual operating conditions, limiting its application in real-world problems [Li, Li, Sun, Luo, and Zhang (2010)]. Uncertainty quantification is, therefore, becoming an increasingly important aspect of the numerical optimization assisted design. Walters and Huyse [Walters and Huyse (2002)] present a comprehensive review of the many approaches developed to quantify uncertainty in simulations, among which the Monte

Carlo Simulation (MCS) is recognized to be the most accurate. The high number of deterministic solutions required to obtain the uncertainty statistics, however, makes its application prohibitive for computationally expensive cfd [Dodson and Parks (2009)]. For such problems more efficient and less computational demanding methods have to be used [Dodson and Parks (2009)].

The second optimization set-up here presented, namely *multi-point*, uses the interval analysis method to account for changes in operating conditions. In particular, the input angle of attack value of the cfd simulation is varied within a specific range to evaluate the variation of the airfoil aerodynamic performance. A similar approach has been used by Srinath in [Srinath, Mittal, and Manek (2009)] for the optimization of a single element airfoil. Three values of α have been chosen within the range $[\alpha_1 - 1^\circ; \alpha_1 + 1^\circ]$ to define the two objective functions expressed in Eq. 3. The first objective function relates to the overall performance of the configuration in the range of angle of attack considered, leading the optimizer to explore designs that increase the *cl* value of the three operating points $\alpha_1 - 1^\circ$, α_1, and $\alpha_1 + 1^\circ$. The second objective function, instead, introduces the concept of robust design, trying to minimize the variation of the lift coefficient with angle of attack. It is evident the inherent multi-objective nature of any robust optimization problem. A constraint on the drag coefficient is applied through the penalty function P. Such a penalty is active only when the sum of the drag coefficient at the three operating points is higher than the datum value.

$$\begin{aligned}
\text{obj1} &= -\frac{cl|_{\alpha_1-1} + cl|_{\alpha_1} + cl|_{\alpha_1+1}}{(cl|_{\alpha_1-1} + cl|_{\alpha_1} + cl|_{\alpha_1+1})|_0} + P \\
\text{obj2} &= \frac{\|cl|_{\alpha_1} - cl|_{\alpha_1-1}\| + \|cl|_{\alpha_1+1} - cl|_{\alpha_1}\|}{(\|cl|_{\alpha_1} - cl|_{\alpha_1-1}\| + \|cl|_{\alpha_1+1} - cl|_{\alpha_1}\|)|_0} + P \\
P &= \max\left[0, \frac{1}{2}\left(\frac{cd|_{\alpha_1-1} + cd|_{\alpha_1} + cd|_{\alpha_1+1}}{(cd|_{\alpha_1-1} + cd|_{\alpha_1} + cd|_{\alpha_1+1})|_0} - 1\right)\right]
\end{aligned} \tag{3}$$

Indeed, this optimization setup represents a much more challenging task compared with the single-point. First of all, in order to achieve the desired performance improvements, the stall characteristic of the airfoil has to be modified. Elements deployment settings can only partially influence the behavior of the airfoil near the maximum lift region. As a consequence, flap shape modification has been included within the optimization process using the free form deformation parameterization technique described earlier. Finally, the increase of both the number of design point evaluations and design variables leads to a considerable rise in computational cost.

5 Results

5.1 Single-Point Optimization

The numerical results of the single-point optimization process after 164 iterations, corresponding to 1217 objective functions evaluations, are here presented. The time required for a single candidate cfd simulation is about 40 minutes, and an average of 8.5 objective functions evaluations (up to 11) for iteration are required. To reduce wall-clock run time the design tool was run on a eight-node parallel PC cluster of 3.0 GHz Intel 5160 Xeon dual-core machines, exploiting the multi-level parallelization capability of the tool. The residual improvement in objective functions has been selected as stopping criteria, resulting in a 450 hours turn around time.

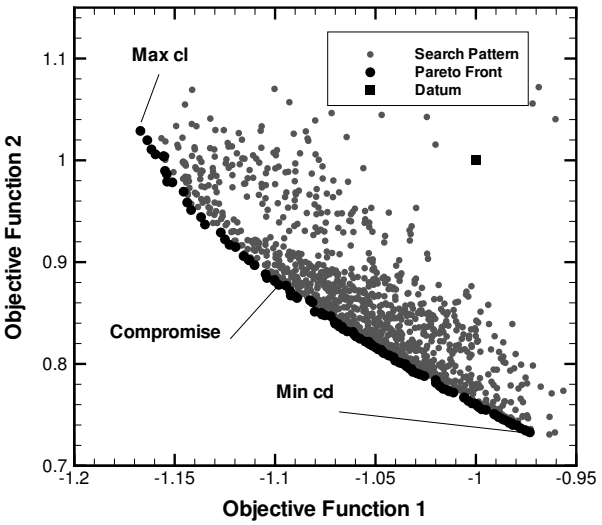

Figure 11: Pareto Front and Search Pattern revealed after 164 iterations. Single-point optimization.

Fig. 11 shows the calculated pareto front, together with the optimization search pattern. The trade-off between the competing objective functions is clearly captured. Three optimum solutions from the pareto front are analyzed in more details and compared with the datum to gain a better understanding of the physics that lead to the performance improvements. In particular, the too extreme optima, representing maximum (normalized) lift coefficient and minimum (normalized) drag coefficient

Table 2: Design variables and objective functions improvement for the optimum designs. Single-point optimization.

	Max_cl	Compromise	Min_cd
Δobj1	-16.7%	-9.6%	1.2%
Δobj2	$+2.9\%$	-11.6%	-24.7%
Δx_S	-0.0178	-0.0178	-0.0178
Δy_S	-0.033	-0.023	-0.023
Θ_S	4°	9°	10°
Δx_F	-0.009	0.011	0.011
Δy_F	0.045	0.045	0.045
Θ_F	4°	-1°	-9°

and a compromise solution are selected. The values of the objective functions for the above mentioned designs are provided in Tab. 2.

The identified optimum designs are illustrated in Fig. 12 together with the datum airfoil. Although each configuration presents peculiar features, some common trends can be identified from the plots. Firstly, all the optimum solutions increase the gap and lap values of both the slat and flap elements compared with the datum design. This characteristic is especially true for the max_cl configuration, which presents the higher separation between the airfoil elements. Secondly, the deflection angle of the slat is consistently increased amongst all the optima. On the contrary, a contrasting trend is observed for the flap deflection angle, which is reduced for the min_cd design and increased for both the compromise and max_cl solutions. The changes in deployment settings are reflected in the elements pressure distribution, shown in Fig. 13. For all the optima design the increased spacial separation between slat and main wing leads to a reduction of the slat effectiveness and a consequent reduction in its aerodynamic load. The opposite trend is observed for the flap element, whose effectiveness is instead increased. As a result, both the flap and main wing aerodynamic loads are higher than the datum configuration ones.

As shown in Tab. 2, the max_cl design achieves a 16.7% increase in the lift coefficient with a drag penalty as low as 2.9%. This considerable performance gain is achieved increasing the deflection angle of both slat and flap by 4 degrees. The resulting lift polar, illustrated in Fig. 14, presents a slightly higher value for the angle of attack of maximum lift (slat effect) and an upward shift (flap effect) compared to the datum. The drag performance is similar to the datum design in the range of angle of attack near α_1. However, for lower angle of attack the drag coefficient is higher than the datum. As a result of these trends the lift to drag ratio of the max_cl

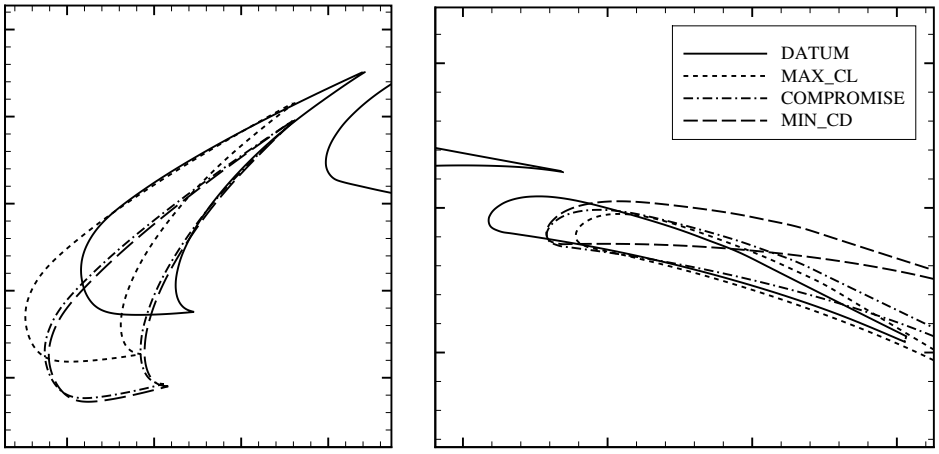

Figure 12: Optima and datum design geometry comparison. Single-point optimization.

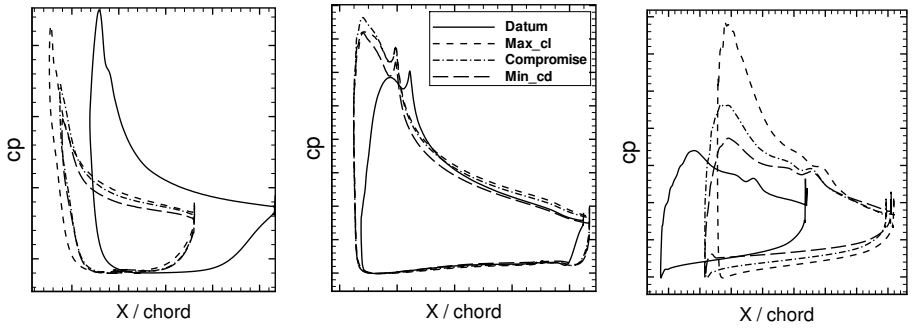

(a) Slat (b) Main (c) Flap

Figure 13: Pressure distributions for datum and optima. Single-point optimization.

design is generally higher than the datum, becoming lower only at moderate angles of attack.

On the contrary, the min_cd design reduces the deflection angle of the flap element by 9 degrees and increases the slat deflection by 10 degrees. The result is a 24.7% decrease in the drag coefficient and only a 1.2% penalty in the lift performance. Again, the flap and slat effects are visible in the lift polar (Fig. 14). A downward shift of the polar is shown together with an increase in the angle of maximum lift. The low drag coefficient values drive the lift over drag performance of the design,

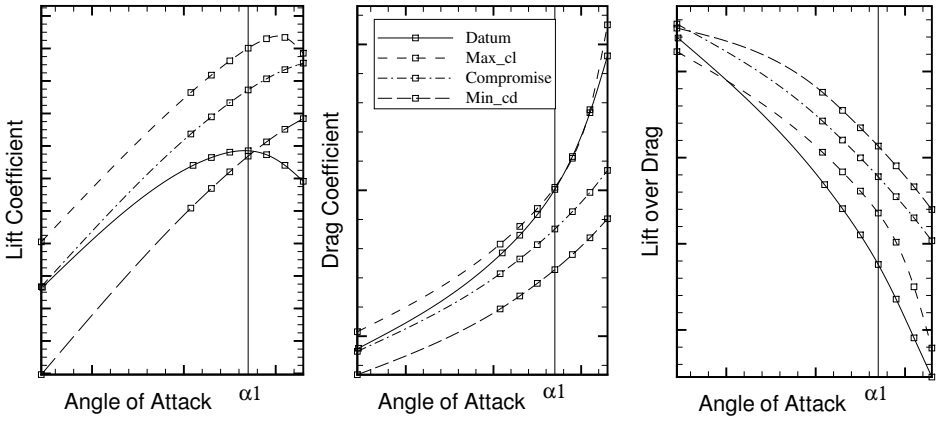

Figure 14: Optima and datum design polar comparison. Single-point optimization.

showing values higher than the datum ones in the whole range of angle of attack considered.

Finally, the compromise solution presents performance levels that lie between the two extreme designs. The deployment settings are similar to the min_cd design, with the only differences being the increased deflection of the flap element and the slight reduction of the slat deflection. This design outperforms the datum configuration in both lift and drag performance for the whole range of angle of attack considered.

The flow field that develops around the analyzed designs is illustrated in Fig. 15. The contour plots show a wide area of high turbulence intensity for the datum configuration generated by the merging of the main element and the flap wakes, followed further downstream by the merging of the slat wake. This flow characteristic leads to a high value for the drag coefficient and an early breakdown in lift. The increased elements gaps of the optima solutions mitigate the described effect, reducing the drag and allowing the airfoil to achieve a greater lift and a higher maximum angle of attack. Nevertheless, the max_cl design shows an increase in the turbulence intensity at the flap trailing edge (as a result of the increased load), indicating an incipient flow separation. This feature limits the maximum angle of attack of this design to a value close to the datum configuration. Such behavior is not visible in the min_cd and compromise designs, which present a much greater maximum angle of attack.

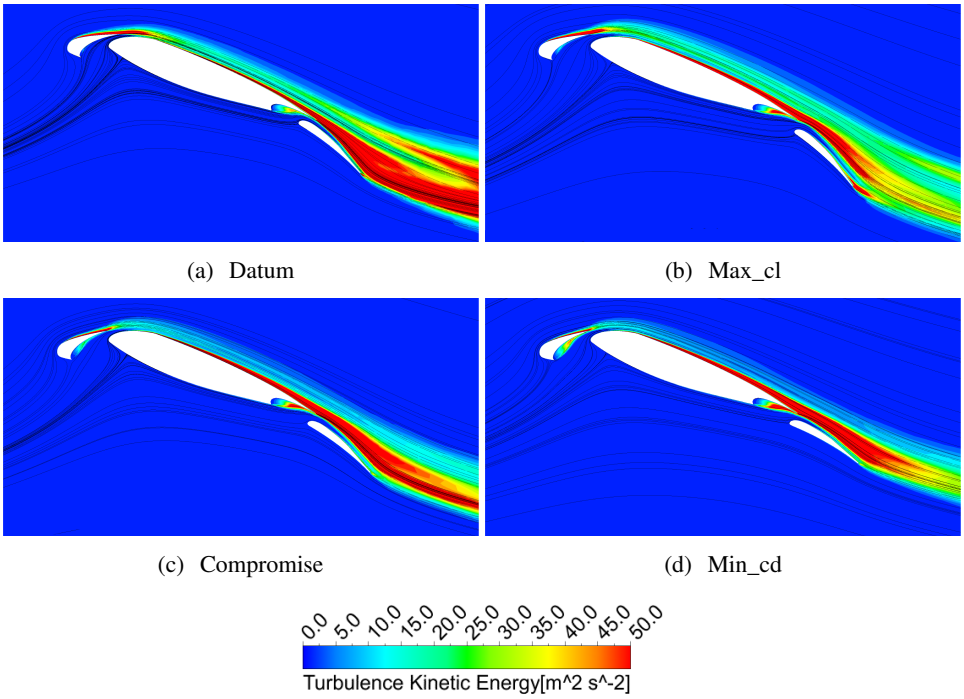

Figure 15: Wake visualization for datum and optimum designs. Single-point optimization.

5.2 Multi-Point Optimization

The results here presented have been extracted from the optimization process after 72 iterations, corresponding to 467 objective functions evaluations. Three times the number of cfd simulations has to be executed to evaluate the objective functions value compared to the single-point case. The increased computational cost combined with the increase in the number of design variables have pushed the turn around time of the complete optimization to around 800 hours. Evaluation time has been selected as the halting criteria for this optimization set-up. The tool was run on a twelve-node parallel PC cluster of 3.0 GHz Intel 5160 Xeon dual-core machines. The time required for a single candidate cfd simulation is around 120 minutes, and an average of 14 objective functions evaluations (up to 28) for iteration are required.

The revealed search pattern and the correspondent pareto front are illustrated in Fig. 16. It can be seen that this specific optimization set-up produces a non-smooth Pareto front, with a discontinuity located in the region of minimum obj1 values.

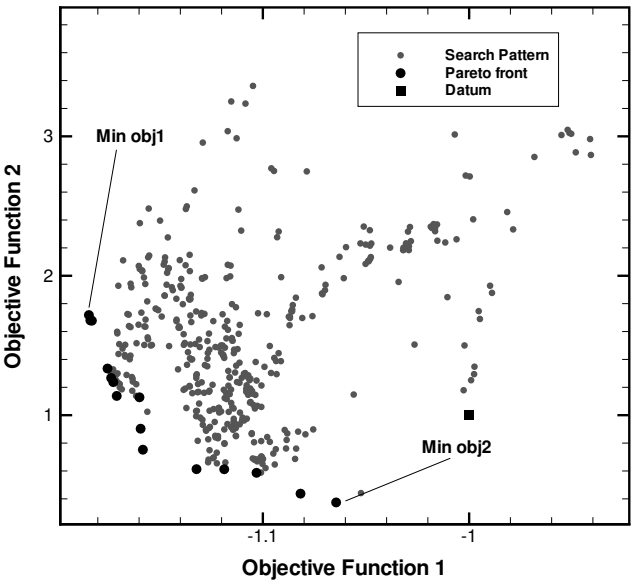

Figure 16: Pareto front and Search Pattern revealed after 72 iterations. Multi-point optimization.

Furthermore, a much higher scatter is found in the Pareto front in comparison with the single-point results. These characteristics reflect the increased complexity introduced in both the design space and objective functions definition. Nonetheless, the MOTS optimization algorithm has been able to identify several optimum designs that improve both objective functions values.

The two extreme optimum solutions from the revealed Pareto front, indicated as min_obj1 and min_obj2, are analyzed in details. The values of the deployment settings for the two optima are reported in Tab. 3, together with the percentage increase in the objective functions. An 18% increase in lift performance is achieved by the min_obj1 design, with a negligible increase in aerodynamic drag (only a 2% value for the penalty function P). However, for the same design, the value of the second objective function is 80% higher than the datum configuration. This behavior can be explained considering the evaluated $cl-\alpha$ polars illustrated in Fig. 18. As it can be seen from the plot, the min_obj1 design presents a higher α_{clmax}, which falls beyond the angle of attack range defined for the optimization process. Therefore, the monotonically increasing segment of the lift curve is used for the evaluation of the objective functions, leading to very different values for the three lift coefficients at $\alpha_1 - 1^\circ$, α_1, and $\alpha_1 + 1^\circ$. The min_obj2 design, instead, shows an improvement in

Table 3: Deployment design variables and objective functions improvement for the optimum designs. Multi-point optimization.

	Min_obj1	Min_obj2
Δobj1	-18.4%	-6.5%
Δobj2	71.2%	-62.6%
Penalty function P	2%	0%
Δx_S	-0.025	-0.005
Δy_S	-0.026	-0.036
Θ_S	7°	2°
Δx_F	0.007	-0.013
Δy_F	0.021	0.021
Θ_F	8°	2°

Table 4: Assessment of operational robustness for the single point optima.

	Min_cd	Compromise	Max_cl
Δobj1	-0.3%	-11.2%	-18.0%
Δobj2	200%	139%	122%

both objective functions (see Tab. 3). The $cl-\alpha$ polar illustrated in Fig. 18 reflects the 6.5% increase in lift, showing an upward shift compared with the datum one. No increase in drag is, however, associated with the augmented lift performance, as shown by the null value of the penalty function P. Moreover, the cl_{max} region of this design falls within the angle of attack range defined for the optimization process. The polar closeup (also shown in Fig. 18) illustrates the increased operational robustness of the optimum solution. In particular, a 63% reduction in the second objective function is achieved by the specific design. Finally, Tab. 4 presents an assessment of the operational robustness of the three optimum designs identified in the single-point optimization set-up (evaluated using Eq. 3). The results show a much lower performance of all the optima compared with the datum design, emphasizing the importance of including robustness formulations within the design process.

The geometrical characteristics that lead to the performance increase are illustrated in Fig. 17. Both the deployments settings and the flap shapes of the two optimum solutions are compared to the datum airfoil. The improvement in lift performance is achieved increasing Δx for both the slat and flap elements, in agreement whit the

results obtained in the single-point optimization. On the contrary, a reduction of the variable Δy_F is observed for both the optima. This translates, for the min_obj2 design, to the positioning of the flap near the trailing edge of the main element. Furthermore, the flap geometries of the two optima show common features: an increase in the element thickness at around 25% chord location and a reduction in the leading edge radius. It is important to point out that these shape changes do not affect the stowed configuration of the airfoil, which retains its cruise shape.

Fig. 19 illustrates the flow-field that develops around the two optimum configurations revealed, at the angle of attack α_1. For both the designs, the reduction in the flap lap reflects in a higher interaction of the main element wake with the flap upper surface. The airflow leaving the main element trailing edge presents a much higher curvature compared to the datum configuration (see Fig. 15 (a)). Such characteristic is emphasized by the shape of the flap element, which promotes the air to flow from the main element pressure side to the flap suction side. However, as a result of this, the main element recirculation bubble is also increased. It is evident that the stall behavior of the configuration is dependent on the interaction between the main element wake and the flap walls. In particular, reduced flap gap settings, characteristic of the min_obj2 design, minimize the variation of lift with angle of attack in the near-stall region. With regard to the changes in slat settings, the same figure shows a much greater influence on the flow-field of the min_obj1 design. The stagnation point in the main wing is shifted aft, and the recirculation bubble in the slat cove region increases. This characteristics are reflected in the lift polar of the specific design, that presents a higher α_{clmax} value.

6 MOTS algorithm performance analysis

The results of the single-point optimization presented earlier have been compared with an identical optimization set-up performed by the authors using the well-known NSGA-II algorithm and a different cfd suite, here indicated as *Cfd_alt*. Tab. 5 summarizes the settings for the two optimization algorithms. The data analyzed has been extracted from the two optimization frameworks at a similar stage of the optimization process (equal number of objective functions evaluations). Fig. 20 illustrates an overlay of the two search patterns and pareto fronts revealed. It is evident that the optimum solutions identified by MOTS fully dominate the NSGA-II ones, apart from a small region located at the extreme minimum obj2. Moreover, the MOTS revealed Pareto front presents a much better spread of the solutions and is more populated. This richness of the Pareto front is one of the limitation of evolution based algorithm, since a maximum size is implicitly set once the number of individuals is fixed [Kipouros, Peachey, Abramson, and Savill (2012)].

A cross validation of three optima from the respective Pareto fronts has been per-

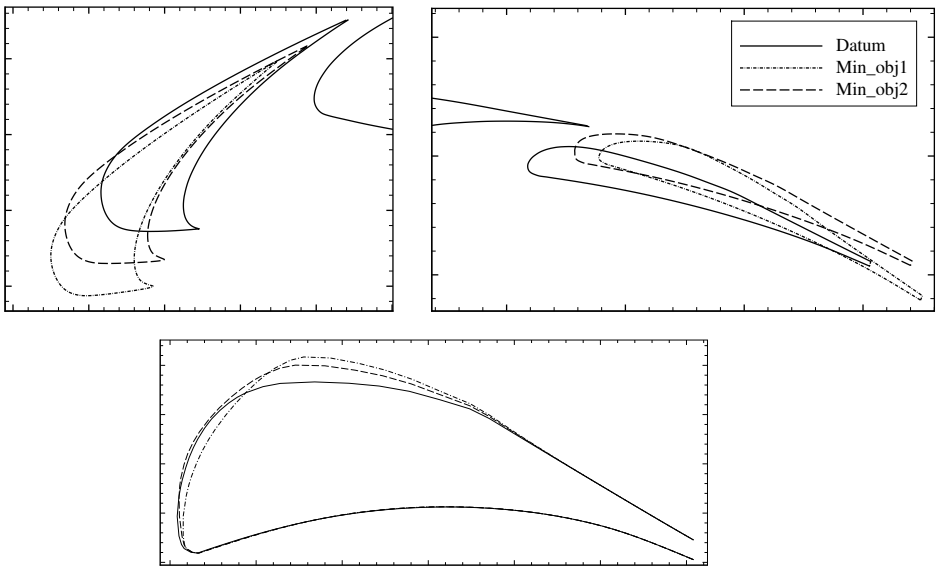

Figure 17: Datum and optima geometry comparison. Close-up of the flap shape changes. Multi-point optimization.

formed to eliminate cfd solver dependencies. The results, illustrated in Fig. 21, show a higher dependency of the MOTS pareto from the cfd suite selected. Nonetheless, MOTS solutions continue to dominate NSGA-II ones but in the case of the min_cd design. Finally, the compromise solution for both MOTS and NSGA-II presents identical objective function values when evaluated with the Cfd_alt solver, although the configuration present different deployment settings. This characteristic is an indication of the complexity and richness of the design space in the tackled aerodynamic design problem.

7 Conclusion

The application of numerical optimization techniques in the design of a multi-element airfoil has here been presented. A realistic test case, the Garteur A310 airfoil, has been selected for the execution of two multi-objective optimization designs. The results of the first optimization set-up, namely *single-point*, have shown that a significant performance gain can be achieved using numerical optimization techniques. A set of different optima has been revealed, from which the designer could select the most suitable configuration. However, such optimum designs are often sensitive to fluctuations in operation conditions. That is why a quantifica-

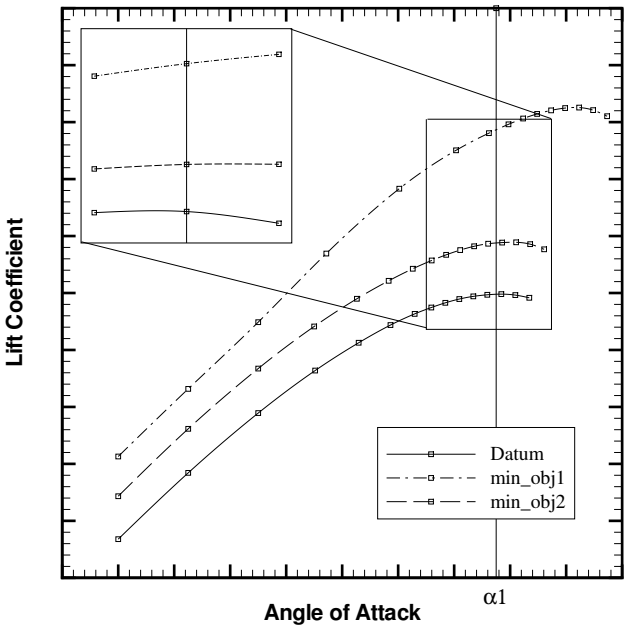

Figure 18: Datum and optima $cl - \alpha$ polars comparison. Multi-point optimization.

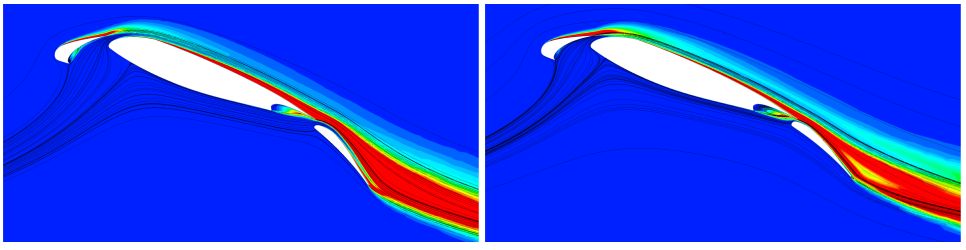

(a) Min_obj1 (b) Min_obj2

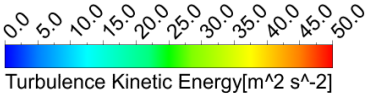

Figure 19: Wake visualization for optimum designs. Multi-point optimization.

Table 5: Optimization Algorithm Settings.

MOTS		NSGAII	
Short Term Memory size	15	Initial Population	48
Long Term Memory size	4	Crossover Probability	0.7
Intensification	15	Mutation Probability	0.17
Diversification	25	Max Generation	100
Step Size Reduction	45	Convergence Generation	5
Max Evaluations	5000	Convergence Threshold	0.001

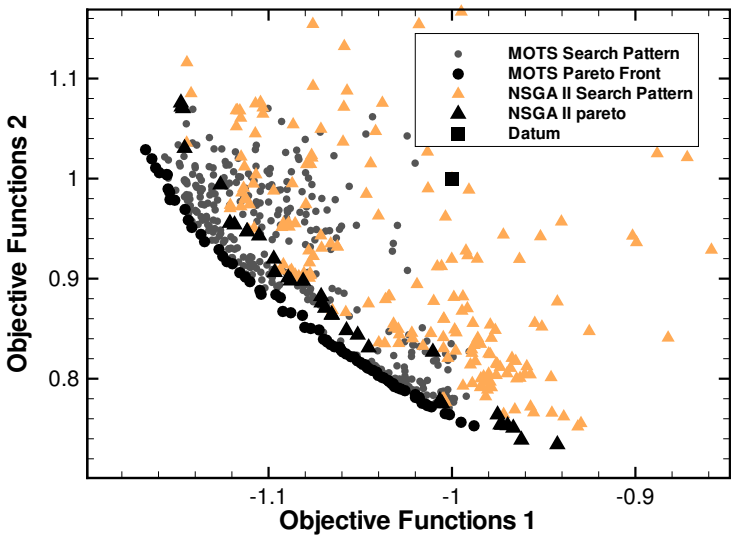

Figure 20: Comparison of Search Pattern and Pareto Front for MOTS and NSGA-II. Single-point optimization.

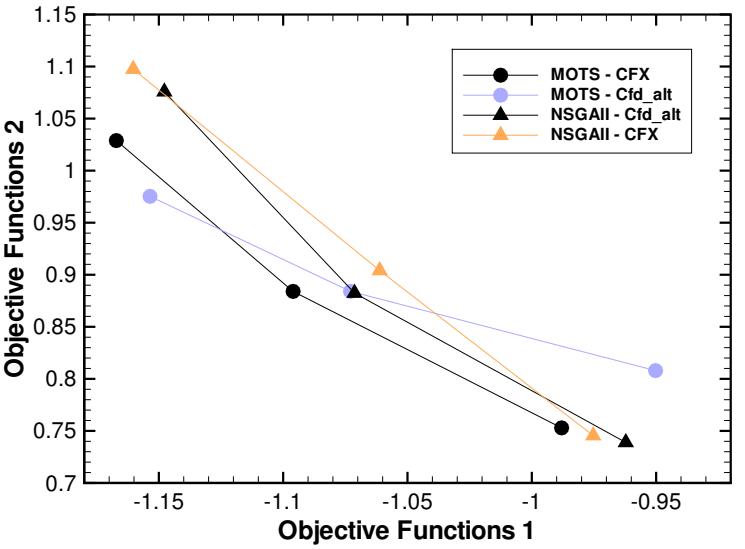

Figure 21: Cross validation of MOTS and NSGA-II Pareto Front. Single-point optimization.

tion of the simulation uncertainty is necessary to operate the design in real-work conditions. The multi-point approach used in the second optimization set-up has been shown to be an efficient strategy to include operational robustness within the optimization process. Using this approach it has been possible to find design that concurrently increase the aerodynamic performance and minimize its variance with angle of attack. Finally, the comparison of the single-point results here presented with an identical optimization set-up performed using the well-known NSGA-II has shown Tabu Search to be an effective and efficient optimization method for aerodynamic problems.

The two optimization processes presented in this work have been performed at a fixed angle of attack. Therefore, future work should focus on implementing a procedure for the automatic identification of the stall angle of attack α_{clmax} for the optimization of maximum lift coefficient. The robust optimization set-up could be expanded including minimization of the variance of the aerodynamic performance on the gap and lap values of the deflected elements. Furthermore, the complexity of the baseline geometry to be optimized could be increased, considering either novel high-lift devices or three-dimensional high-lift configurations. In the latter case low/medium fidelity cfd methods or surrogate models should be used in order to limit the computational cost. Finally, the framework could be expanded to include

multi-disciplinary aspects such as aerodynamic-structure interaction.

Acknowledgement: The lead author G. Trapani acknowledges the EPSRC (Engineering and Physical Sciences Research Council) and Eng. Murray Cross (Technology Product Leader for Future Simulation at Airbus Operations Ltd.) for granting the Engineering Doctorate research project. Furthermore, the lead author gratefully thanks the academic supervisors Dr. Timoleon Kipouros and Prof. A. Mark Savill and the industrial supervisor Eng. Stefano Tursi (Head of Geometry, CAD management and framework at Airbus Operations Ltd.) for their continuous guidance and support.

References

Amoignon, O.; Quest, J.; Moens, F.; Quagliarella, D.; Wild, J. W.; Brezillion, J. (2007): Advanced high-lift design by numerical methods and wind tunnel verification within the european project EUROLIFT II. In *25th AIAA Applied Aerodynamics Conference*, pp. 1–18, Miami, Florida. AIAA.

Bardina, J. E.; Huang, P. G.; Coakley, T. J. (1997): Turbulence modeling validation, testing and development. NASA technical memorandum–110446, NASA, 1997.

Besnard, E.; Schmitz, A.; Boscher, E.; Garcia, N.; Cebeci, T. (1998): Two-dimensional aircraft high lift system design and optimization. In *36th Aerospace Sciences Meeting and Exhibit*, Reno, NV. AIAA–98–0123.

Carrese, R.; Winarto, H.; Li, X.; Sóbester, A.; Ebenezer, S. (2012): A comprehensive preference-based optimization framework with application to high-lift aerodynamic design. *Engineering Optimization*, vol. 44, no. 10, pp. 1209–1227.

Connor, A.; Tilley, D. (1998): A tabu search method for the optimisation of fluid power circuits. *IMechE Journal of Systems and Control*, vol. 212, pp. 373–381.

Deb, K.; Pratap, A.; Agarwal, S.; Meyarivan, T. (2002): Fast and elitist multiobjective genetic algorithm:NSGA-II. *IEEE Transactions on Evolutionary Computation*, vol. 6, no. 2, pp. 182–197.

Diwakar, A.; Srinath, D.; Mittal, S. (2010): Aerodynamic shape optimization of airfoils in unsteady flow. *CMES: Computer Modeling in Engineering & Sciences*, vol. 69, no. 1, pp. 61–89.

Dodson, M.; Parks, G. T. (2009): Robust aerodynamic design optimization using polynomial chaos. *Journal of Aircraft*, vol. 46, no. 2, pp. 635–646.

Edgeworth, F. Y. (1881): *Mathematical Physics*. C. Kegan Paul, London, England.

Eyi, S.; Lee, K. D.; Rogers, S. E.; Kwak, D. (1996): High-lift design optimization using navier-stokes equations. *Journal of Aircraft*, vol. 33, no. 3, pp. 499–504.

Fejtek, I. (1997): Summary of code validation results for a multiple element airfoil test case. In *Proceedings of the 28th AIAA Fluid Dynamics Conference*, pp. 1–15, Snowmass Village, CO. AIAA–97–1932.

Flaig, A.; Hilbig, R. (1993): High-lift design for large civil aircraft. AGARD CP 515, 1993.

Ghisu, T.; Parks, G. T.; Jarrett, J. P.; Clarkson, P. J. (2011): An integrated system for the aerodynamic design of compression systems: part II: Application. *Journal of Turbomachinery*, vol. 133, no. 1, pp. 011012.

Greener by Design Science and Technology Sub-Group (2005): Mitigating the environmental impact of aviation: Opportunities and priorities. Technical report, Royal Aeronautical Society, 2005.

Harvey, S. A. (2002): *The design optimisation of turbomachinery blade rows*. PhD thesis, Cambridge University, 2002.

Huyse, L.; Padula, S. L.; Lewis, M. R.; Wu, L. (2002): Probabilistic approach to free-form airfoil shape optimization under uncertainty. *AIAA Journal*, vol. 40, no. 9, pp. 1764–1772.

Jaeggi, D. M.; Parks, G. T.; Kipouros, T.; Clarkson, P. J. (2008): The development of a multi-objective tabu search algorithm for continuous optimization problems. *European Journal of Operational Research*, vol. 185, pp. 1192–1212.

Kanazaki, M.; Tanaka, K.; Jeong, S.; Yamamoto, K. (2007): Multi-objective aerodynamic optimization of elements' setting for high-lift airfoil using kriging model. *Journal of Aircraft*, vol. 44, no. 4, pp. 854–867.

Kim, S.; Alonso, J. J.; Jameson, A. (2002): Design optimization of high-lift configurations using a viscous continuous adjoint method. AIAA–2002-0844, AIAA, 2002.

Kipouros, T. (2006): *Multi-Objective Aerodynamic Design Optimization*. PhD thesis, Cambridge University, 2006.

Kipouros, T.; Jaeggi, D. M.; Dawes, W. N.; Parks, G. T.; Savill, A. M.; Clarkson, P. J. (2008): Biobjective design optimization for axial compressors using tabu search. *AIAA Journal*, vol. 46 (3), pp. 701–711.

Kipouros, T.; Jaeggi, D. M.; Dawes, W. N.; Parks, G. T.; Savill, A. M.; Clarkson, P. J. (2008): Insight into high-quality aerodynamic design spaces through

multi-objective optimization. *CMES: Computer Modeling in Engineering and Sciences*, vol. 37, no. 1, pp. 1–44.

Kipouros, T.; Peachey, T.; Abramson, D.; Savill, A. M. (2012): Enhancing and developing the practical optimisation capabilities and intelligence of automatic design software. In *8th AIAA Multi-Disciplinary Design Optimization Specialist Conference, Honolulu, Hawaii*. AIAA–2012–1677.

Kroll, N.; Gauger, N. R.; Brezillon, J.; Dwight, R.; Fazzolari, A.; Vollmer, D.; Becker, K.; Barnewitz, H.; Schulz, V.; Hazra, S. (2007): Flow simulation and shape optimization for aircraft design. *Journal of Computational and applied mathematics*, vol. 203, pp. 397–411.

Li, F.; Li, G.; Sun, G.; Luo, Z.; Zhang, Z. (2010): Multi-disciplinary optimization for multi-objective uncertainty design of thin walled beams. *CMES: Computer Modeling in Engineering & Sciences*, vol. 19, no. 1, pp. 37–56.

Lian, Y. S.; Liou, M. S. (2005): Mining of data from evolutionary algorithms for improving design optimization. *CMES: Computer Modeling in Engineering & Sciences*, vol. 8, no. 1, pp. 61–67.

Lindblad, I. A. A.; de Cock, K. M. J. (1999): Cfd prediction of maximum lift of a 2d high lift configuration. In *Proceedings of the 17th AIAA Applied Aerodynamics Conference*, pp. 1–13, Norfolk, VA. AIAA–99-3180.

Manie, F.; Piccini, O.; Ray, J. P. (1989): Test report of the 2d model m1 in the onera f1 wind tunnel. GARTEUR high lift Action Group AD (AG-08) TP041, GARTEUR, 1989.

Murayama, M.; Yamamoto, K. (2005): Validation of flows on high-lift configurations by structured and unstructured mesh method. In *43rd AIAA Aerospace Science Meeting and Exhibit*, pp. 1–15, Reno, Nevada. AIAA 2005-1226.

Nemec, M.; Zingg, D. W.; Pulliam, T. H. (2004): Multipoint and multiobjective aerodynamic shape optimization. AIAA Journal 6, AIAA, 2004.

Pareto, V. (1896): *Cours D'Economie Politique*, volume I and II. F. Rouge, Lasusanne.

Rudnik, K.; Eliasson, P.; Perraud, J. (2005): Evaluation of cfd methods for transport aircraft high lift systems. *The Aeronautical Journal*, vol. 109, pp. 53–64.

Rudolph, P. K. C. (1996): High-lift systems on commercial subsonic airliners. NASA cr–4746, NASA, 1996.

Rumsey, C. L.; Ying, S. X. (2002): Prediction of high lift: review of present cfd capability. *Progress in Aerospace Sciences*, vol. 38, pp. 145–180.

Sederberg, T. W.; Parry, S. R. (1986): Free-form deformation of solid geometric models. *SIGGRAPH*, vol. 20, no. 4.

Smith, A. M. O. (1975): High-lift aerodynamics. *Journal of Aircraft*, vol. 12, no. 6, pp. 501–530.

Srinath, D. N.; Mittal, S.; Manek, V. (2009): Multi-point shape optimization of airfoils at low reynolds numbers. *CMES: Computer Modeling in Engineering & Sciences*, vol. 51, no. 2, pp. 169–188.

van Dam, C. P. (2002): The aerodynamic design of multi-element high-lift systems for transport airplanes. *Progress in Aerospace Sciences*, vol. 38, pp. 101–144.

Walters, R. W.; Huyse, L. (2002): Uncertainty analysis for fluid mechanics with applications. NASA CR–2002–211449, NASA, 2002.

Wild, J. W. (1998): Direct optimization of multi-element-airfoil for high-lift using navier-stokes equations. In *4th European Computational Fluid Dynamics Conference Part1*, pp. 383–390, Athens, Greece. John Wiley and Sons Ltd.

Wild, J. W. (2008): Multi-objective constrained optimization in aerodynamic design of high-lift system. *International Journal of Computational Fluid Dynamics*, vol. 22, no. 3, pp. 153–168.